Pressure-induced superconductivity and enhanced optoelectronic property in the ternary pentagonal semiconductor PdPSe

Nixian Qian [1,2] Zheng Chen,[1] Yonghui Zhou,[1,2,*] Liangyu Li,[1,2] Chunhua Chen,[1] Shuyang Wang,[1] Ranran Zhang,[1] Xuliang Chen,[1,2] Chao An,[3] Ying Zhou,[3] Min Zhang,[3] Xiaoping Yang,[1,2,†] and Zhaorong Yang[1,2,3,4,‡]

[1]*Anhui Key Laboratory of Low-Energy Quantum Materials and Devices, High Magnetic Field Laboratory, HFIPS, Chinese Academy of Sciences, Hefei 230031, China*
[2]*Science Island Branch of Graduate School, University of Science and Technology of China, Hefei 230026, China*
[3]*Institutes of Physical Science and Information Technology, Anhui University, Hefei 230601, China*
[4]*Collaborative Innovation Center of Advanced Microstructures, Nanjing 210093, China*

The ternary van der Waals (vdW) pentagonal semiconductor PdPSe has gathered significant attention due to its unique anisotropic structure and exotic optoelectronic properties originating from the distinct Cairo pentagonal tiling topology. Here, we report pressure tuning of the photoelectronic and electronic properties of pentagonal PdPSe. We show that the photocurrent is enhanced by over two orders of magnitude at 25.9 GPa and suddenly disappears upon further compression. Meanwhile, metallization and superconductivity simultaneously occur at around 25 GPa. The superconducting critical temperature T_c initially increases and then becomes robust up to ~60 GPa. Synchrotron x-ray diffraction and Raman experiments consistently indicate the disappearance of photocurrent and the occurrence of superconductivity are both correlated to the formation of a high-pressure amorphous phase. As a result of the irreversible nature of the amorphization, metallic conductivity retains near ambient pressure in depressurized PdPSe. The synchronous evolution of structural, photoelectronic, and electronic properties elucidates a deep understanding of the structure-property relationship and emergent functionalities in a vdW pentagonal semiconductor via pressure modulation. This finding further provides an opportunity for tuning, understanding, and exploring the related vdW pentagonal materials under extreme conditions.

I. INTRODUCTION

Since the discovery of graphene in 2004, two-dimensional (2D) materials have rapidly advanced in material design, production, and application [1,2]. Numerous investigations have expanded the family of 2D materials beyond the conventional hexagonal structure and improved the understanding of the composition-structure-property relationship therein. In 2015, Zhang *et al.* theoretically proposed a novel 2D carbon allotrope named penta-graphene, which is constructed of carbon atoms with a Cairo pentagonal tiling [3]. The introduction of pentagon atom configurations results in ultrahigh ideal strength and wide intrinsic band gap in penta-graphene [3]. Since then, a great deal of effort has been devoted to the design and synthesis of 2D pentagon-based materials, spanning from the unitary to binary, and ternary systems [4,5]. Theoretical analyses and experiments demonstrated that owing to their unique geometries, pentagonal materials host intriguing physical properties, such as negative Poisson's ratio, spontaneous polarization, intrinsic piezoelectricity, and out-of-plane second harmonic generation responses [3–9].

Specifically, as the first synthesized pentagonal compound, $PdSe_2$ is air stable and has been expected to be a next generation candidate for applications in optoelectronics and anisotropic optics, due to its puckered pentagonal structure and resultant layer-dependent tunability, highly anisotropic, ultrawide spectral range, and highly polarization-sensitive photoresponse [10–12]. Recently, Duan *et al.* designed the ternary pentagonal semiconductor PdPSe by the fusion of black phosphorus and $PdSe_2$ [13]. As a derivation of $PdSe_2$ (orthorhombic, *Pbca*), PdPSe crystallizes in orthorhombic structure (*Pbcn*), where two PdPSe sublayers are bonded by P-P bonds to form a single molecular layer and stack along the *a* axis [Fig. 1(a)] [13,14]. The synthesized pentagonal PdPSe has excellent air stability due to the strong hybridization between noble metals and chalcogens, along with high on/off ratio and excellent photoresponse [13–15]. Its photoelectronic property and band gap are sensitive to the layer thickness, e.g., the on/off ratio varying from 10^5 of 9.65 nm to 10^8 of 6.9 nm [14] and the band gap varying from 1.43 eV of bulk to 1.97 eV of monolayer [16]. In addition, the physical properties of PdPSe can be effectively modulated by external stimulants, such as light, electric, strain, and molecular adsorption [13,14,16,17].

Pressure is an effective and clean method to tune the structural and physical properties and to induce novel physical phenomena, such as band-gap regulation, photocurrent gain,

*Corresponding author: yhzhou@hmfl.ac.cn
†Corresponding author: xpyang@hmfl.ac.cn
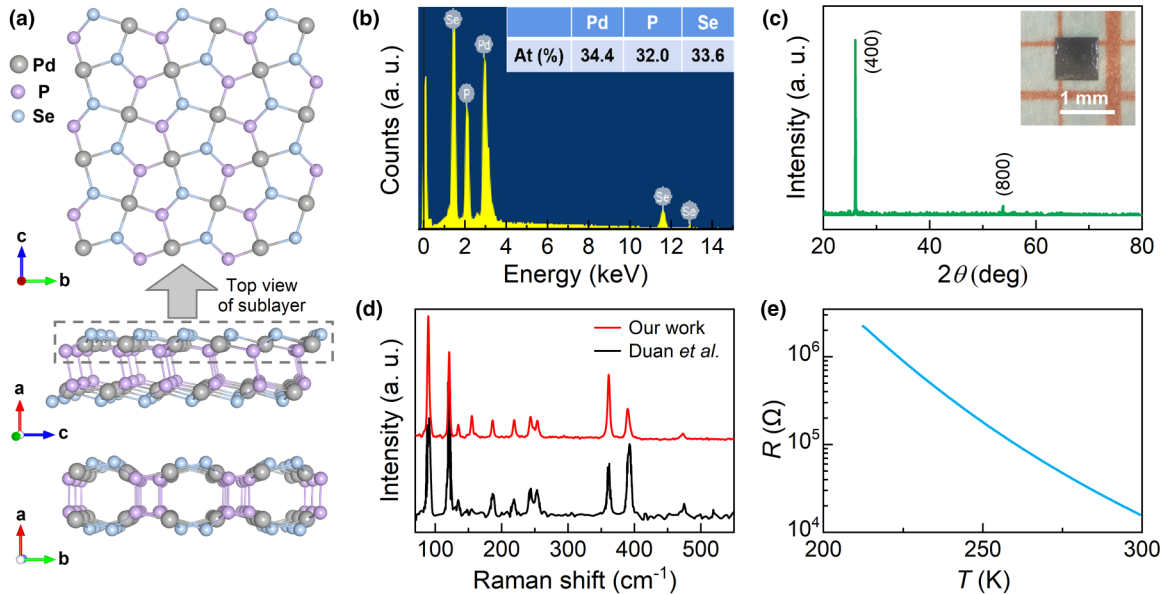‡Corresponding author: zryang@issp.ac.cn

FIG. 1. Structural characterization and physical properties at ambient pressure. (a) Schematic crystal structure of PdPSe at ambient conditions. Results of PdPSe single crystals: EDXS (b), XRD (c), Raman spectrum (d), resistance-temperature curve (e).

ambipolar modulation, and superconductivity [18–21]. Compared with intensive investigations of typical 2D materials under pressure, the high-pressure study of penta-based materials is very limited. The binary penta-based compound, $PdSe_2$, undergoes an orthorhombic-to-cubic transition (*Pbca* to *Pa*3) above 6 GPa, concomitant with the appearance of metallization and superconductivity [22,23]. Theoretical calculation indicated that PdPS will undergo a semiconductor-metal transition at 24 GPa and an orthorhombic-monoclinic phase transition between 30 and 32 GPa [24]. To date, the pressure effect on the structure-property relationship of ternary penta-PdPSe remains elusive.

In this work, we systematically investigated the pressure evolution of the structural, photoelectronic, and electronic properties of the optical semiconductor penta-PdPSe. X-ray diffraction and Raman-scattering experiments reveal that PdPSe undergoes a crystalline-to-amorphous transition around 25 GPa, which is accompanied by the occurrence of metallization and superconductivity and the sudden disappearance of photocurrent. In line with the irreversible structural transition, the evolution of electronic properties is also irreversible.

II. MATERIALS AND METHODS

PdPSe single crystals were synthesized by the chemical vapor transport method. Pd, P, and Se with a 1:1:1 ratio and 100 mg I_2 were sealed into a vacuum quartz tube and then the tube was transferred to a two-zone furnace. Two zones were slowly heated up to 900 °C and 950 °C, respectively, and preserved for 24 h. Then, it was turned around two zones and transported at 910 °C and 850 °C for 7 days, respectively. After cooled down to room temperature, the square-shaped PdPSe single crystals were collected from the quartz tube. Room-temperature x-ray diffraction (XRD) patterns of single crystal were

obtained with Cu $K\alpha$ radiation ($\lambda = 1.5406$ Å) using a Rigaku x-ray diffractometer (Miniflex-600). The atomic proportion of crystal was confirmed by energy dispersive x-ray spectroscopy (EDXS; Helios Nanolab 600i, FEI) with area-scanning mode. The Raman spectrum was recorded in a Renishaw spectrometer with pseudo backscattering configuration ($\lambda = 532$ nm). Electrical transport measurements were carried out in a physical property measurement system (Quantum Design).

The measurement details are similar to Ref. [25]. The culet of the diamond was 300 μm. The high-pressure photocurrent was measured with a Keysight B2912A source meter, and the center position between two Pt/Au probes was selected to be illuminated with a 532-nm excitation laser at the power of 45 mW. NaCl was used as the pressure-transmitting medium (PTM) in electrical measurements. Electrical transport measurements were performed by four-probe configuration. The applied magnetic field was perpendicular to the surface of the flake. Powder angle-dispersive synchrotron XRD experiment was carried out at beamline BL15U1 of Shanghai Synchrotron Radiation Facility ($\lambda = 0.6199$ Å), where silicone oil was used as the PTM. Raman spectra were recorded on flake PdPSe surfaces by using a Renishaw spectrometer with pseudo backscattering configuration ($\lambda = 532$ nm). The laser power was kept below 2.5 mW to avoid sample damage and heating effect. The backscattered signal was collected in an unpolarized geometry through 20× objective and 1800 g/mm grating. Pressure was calibrated by the ruby fluorescence shift at room temperature in all high-pressure experiments [26].

Based on the Perdew-Burke-Ernzerhof exchange-correlation functional and the projected augmented wave method [27,28], ground state energy was calculated by using the Vienna *ab initio* simulation package (VASP) [29]. The energy cutoff was 400 eV, and the spacing between neighboring k points in momentum space was 0.015 Å^{-1}. The crystal structure parameters were optimized using the
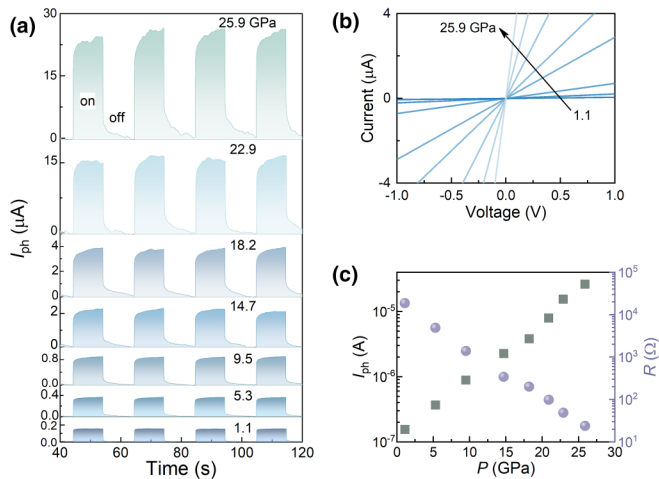
FIG. 2. Pressure-tuned photoelectronic properties of PdPSe single crystals via $V_{ds} = 1.0$ V. (a) I_{ph} as a function of time at different pressures with a wavelength of 532 nm from 1.1 to 25.9 GPa. (b) The I-V curves of the PdPSe device measured in the dark at different pressures. (c) Pressure dependence of photocurrent I_{ph} and the room-temperature resistance $R_{300\,K}$ of PdPSe.

conjugate gradient technique with a force convergence criterion of 0.001 eV/Å. The phonon vibrational frequency was investigated by using the density functional perturbation theory which constructs the force-constant matrix. Then we can obtain the dynamical matrix by a Fourier transformation [30]. The phonon frequencies and vibrational modes can be obtained by diagonalizing the dynamical matrix directly using the PHONOPY code [31].

III. RESULTS AND DISCUSSION

The characterization of structural and physical properties of PdPSe single crystals were performed by multiple experimental measurements at ambient pressure. As shown in Fig. 1(b), the EDXS result yields a composition of PdP$_{0.93}$Se$_{0.97}$. Figure 1(c) shows the XRD pattern of PdPSe single crystal. Only (h00) diffraction peaks can be detected and indexed, indicating that the bc plane is the natural cleavage facet. The inset of Fig. 1(c) displays a typical optical image of as-grown PdPSe single crystal. The room-temperature Raman spectrum in Fig. 1(d) reveals several Raman peaks in the range of 70–550 cm^{-1}, which is consistent with previous reports [13]. Figure 1(e) shows the resistance-temperature $R(T)$ curve from 300 to 210 K, which can be fitted by the Arrhenius model $\rho(T) = \rho_0 \exp(E_g/k_B T)$, where k_B and E_g are the Boltzmann constant and thermal activation energy, respectively. The extracted activation energy E_g is $\sim$0.14 eV, comparable with those of early literature [32,33]. All the results indicate the high quality of our samples.

To explore the pressure effect on the photoelectronic property of PdPSe single crystals, we measured the room-temperature photoelectric response of the PdPSe device at various pressures. As shown in Fig. 2(a), PdPSe exhibits a typical photoresponse between 1.1 and 25.9 GPa, along with multiple cycles of on-off switching behavior. Upon

compression, the photocurrent of the device significantly increases. According to the definition of the responsivity $R = I_{ph}/PS$ (where I_{ph}, P, and S are the difference of current between light and dark environment, light intensity, and irradiation area, respectively), the responsivity can be derived as being proportional to I_{ph} [34]. One can see that the photocurrent increases with further increasing pressure up to 25.9 GPa. However, the photocurrent abruptly disappears upon further compression. As shown in Fig. 2(b), the $I(V)$ curves at high pressures show a linear feature, signaling good Ohmic contact between sample and Pt/Au electrodes during the experiments. Pressure-dependent I_{ph} and room-temperature resistance $R_{300\,K}$ are plotted together in Fig. 2(c). The maximum I_{ph} is $\sim$26.4 μA at 25.9 GPa, which is 169 times larger than the initial $\sim$156 nA at 1.1 GPa. This enhancement of photocurrent in PdPSe exceeds previously reported enhancements of most transition metal dichalcogenide materials under high pressure [21,35–37]. In general, electrons in the valence band become easily excited to the conduction band when the band gap decreases, giving rise to larger photocurrent intensity [35,37]. Indeed, $R_{300\,K}$ shows a large decrement from $\sim$19 kΩ at 1.1 GPa to $\sim$20 Ω at 25.9 GPa, indicating the great enhancement of conductivity under high pressure. Note that some pressure-treated perovskites show a close relationship between the enhancement of optoelectrical properties and the improvement of structural stabilities [38]. The absence of a detectable photocurrent signal over $\sim$26 GPa is possibly related to the occurrence of metallization and/or structural change under compression.

Electrical transport measurements with four-probe configuration were further performed to verify the possibility of metallization in pressurized PdPSe. The representative resistance-temperature $R(T)$ curves are shown in Fig. 3(a). At 0.8 GPa, PdPSe exhibits a semiconducting behavior, reflected by the increment of resistance upon cooling. With increasing pressure, the resistance decreases over the whole temperature range and a metallic conductivity is indeed observed at 24.0 GPa. Meanwhile, the appearance of metallization is concomitant with a distinct resistance drop at $\sim$3.2 K [Fig. 3(b)]. Further increased pressure gives rise to the observation of zero resistance at 28.5 GPa, indicating the presence of pressure-induced superconductivity. The superconductivity enhances to the highest pressure of 57.2 GPa. The upper critical magnetic field at 48.6 GPa is characterized by varying the external magnetic field. As shown in Fig. 3(c), the superconducting transition is gradually smeared out by increasing the magnetic field up to 5.0 T. By defining the T_c value as the 90% drop of the normal-state resistance, the temperature-magnetic-field phase diagram at 48.6 GPa was constructed in Fig. 3(d). The upper critical field extracted by Ginzburg-Landau (GL) model fitting is 4.53 T, which is far less than the Pauli limiting value of $\mu_0 H_p(0) = 1.84 T_c$, indicating the absence of Pauli pair breaking [39]. Hall resistance measurement was simultaneously conducted to trace the charge-carrier evolution versus pressure. Figure 3(e) shows the transversal Hall resistance R_{xy} as a function of magnetic field at 10 K and various pressures. All $R_{xy}(H)$ curves display a quasilinear behavior with a negative slope, indicating that the electron-type carriers dominate the transport behavior of PdPSe at high pressures. According to a single band model, electron carrier
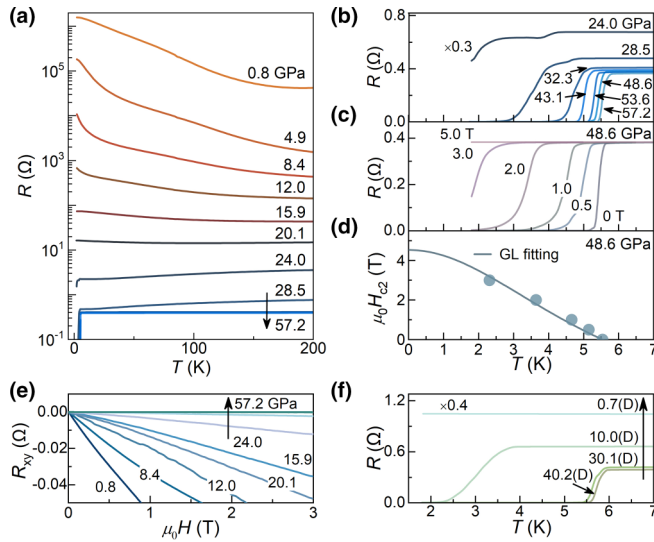
FIG. 3. Electrical transport property of PdPSe under high pressure. (a) Representative resistance-temperature $R(T)$ curves of PdPSe single crystal up to 57.2 GPa. (b) Enlarged view of $R(T)$ curves below 7 K. (c) $R(T)$ curves under different magnetic fields at 48.6 GPa. (d) Temperature-dependent upper critical field ($\mu_0 H_c$) at 48.6 GPa. T_c value at specific magnetic field is defined by a 90% drop of the normal-state resistance. The black solid line represents the GL fitting. (e) Typical transversal Hall resistance R_{xy} as a function of magnetic field at 10 K from 0.8 to 57.2 GPa. For clarity, the resistance R_{xy} for 0.8, 8.4, and 12.0 GPa have been multiplied by the factor of 0.006, 0.03, and 0.2, respectively. (f) Low-temperature $R(T)$ curves under decompression (denoted by "D").

density n_e was extracted at the low-field limit, which will be discussed below. The transport behavior was also investigated during decompression, as illustrated in Fig. 3(f). One can see that the superconductivity is gradually suppressed upon decompression. When the pressure is released to 0.7 GPa, superconducting transition cannot be observed upon cooling down to 1.8 K. But the metallic conductivity is still preserved. It thus demonstrates the irreversibility of transport properties after a compression-decompression cycle in pressurized PdPSe.

Next, we carried out powder angle-dispersive synchrotron XRD experiments to explore the stability of the crystal structure of PdPSe. Figure 4(a) shows the representative XRD patterns at various pressures. The XRD data below 30.2 GPa can be indexed by the pristine orthorhombic structure with space group *Pbcn* (No. 60) via the Le Bail method. The fitting result at 0.3 GPa is given at the bottom of Fig. 4(a). Due to lattice contraction, all peaks shift to high angles upon compression. Above 30.2 GPa, however, most of the diffraction peaks become much broader along with the large reduction in peak intensity, indicating the presence of amorphization. At 38.6 GPa, the XRD pattern only displays two broad diffusive peaks around 15.6° and 20.7°. Notably, the amorphous phase is captured after releasing the pressure to 0.7 GPa. The irreversible structure evolution is in accordance with the irreversibility of conductivity as mentioned above [Fig. 3(f)].

For crystalline PdPSe, the lattice parameters and volume were extracted and plotted in Figs. 4(b) and 4(c). As pressure increases up to 30.2 GPa, the parameters a, b, and c are reduced by 13.1%, 3.0%, and 3.7%, respectively. The
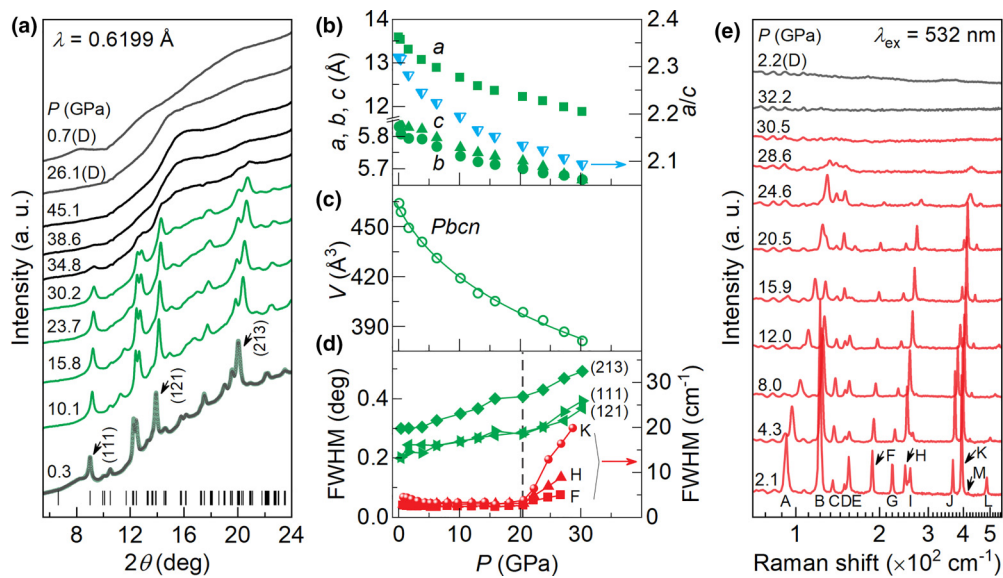

FIG. 4. Angle-dispersive synchrotron XRD patterns and Raman spectra of PdPSe under high pressure. (a) Typical powder synchrotron XRD patterns at room temperature ($\lambda = 0.6199$Å) under compression and decompression (denoted by "D"). The typical refinement with space group *Pbcn* (No. 60) is shown at 0.3 GPa with $R_p = 0.78\%$, $R_{wp} = 1.43\%$. Peak positions are shown as vertical bars. (b) The pressure-dependent lattice parameters a, b, c, and axis ratio a/c. (c) The volume as a function of pressure. The solid line is the fittings according to the third-order Birch-Murnaghan equation of state. (d) Pressure evolution of FWHM of the representative XRD diffraction peaks [(111), (121), and (213); left axis] and Raman modes (F, H, and K; right axis). (e) Room-temperature Raman spectra of PdPSe single crystal under compression and decompression (denoted by "D"). The English letters denote the Raman modes.

axis ratio a/c decreases continuously, indicating a significant compressibility of interlayer spacing in layered PdPSe. The volume as a function of pressure can be fitted by the third-order Birch-Murnaghan equation of state [40], as indicated by the solid lines in Fig. 4(c). The fitting result yields bulk modulus $B_0 = 66.68$ GPa, first-order derivative of the bulk modulus at ambient pressure $B_0' = 7.73$, and ambient-pressure volume $V_0 = 461.33$ Å^3, respectively.

Since Raman spectroscopy is an effective method to investigate the lattice dynamics, vibrational properties, and structure evolution, we further carried out Raman-scattering experiment on PdPSe single crystal. Figure 4(e) presents room-temperature Raman spectra measured up to 32.2 GPa. Pristine PdPSe belongs to space group *Pbcn* and point group D_{2h}, and group theory analysis yielded 36 Raman-active modes, i.e., $9(A_g + B_{1g} + B_{2g} + B_{3g})$ [14,24]. Thirteen Raman modes, located at 92.02, 121.88, 135.57, 149.21, 154.78, 187.92, 222.13, 246.85, 257.27, 366.61, 394.18, 415.71, and 485.31 cm^{-1}, are detected at 2.1 GPa in the frequency range of 70–550 cm^{-1}. These Raman modes are labeled by letters from A to L, respectively. Our calculations indicate that most of the Raman modes can be assigned as A_g (E, H, J, K, and L), B_{1g} (B and F), B_{2g} (G), and B_{3g} (C), similar to the previous literature [14,41]. Furthermore, we found that A, I, and M are related to the B_{1g} or B_{3g} mode, while D belongs to the B_{2g} mode. With increasing pressure, the modes are continuously shifted toward a higher wave number. Notably, the intensity of major Raman modes declines above 20.5 GPa and finally becomes undetectable above 30.5 GPa. The FWHM of three representative Raman modes is plotted together with three representative XRD diffraction peaks in Fig. 4(d). One can see that an anomaly occurs around 20.5 GPa, which suggests the precursor of structural instability. Note that the featureless Raman spectra appear above 30.5 GPa within the high-pressure amorphous PdPSe, which behaves as a metallic conductivity [Fig. 3(a)]. Given that a reduced Raman cross section is expected for metallic systems compared to insulators [42], we suggest that the featureless Raman spectra here are correlated to the presence of a metallic high-pressure amorphous phase. Furthermore, owing to the irreversibility of the crystalline-amorphous transition and the preservation of amorphization in a depressurized sample, the Raman spectrum is also featureless after decompression. The discrepancy of critical transition pressures between the electrical and structural experiments could be attributed to the pressure distribution due to the difference in pressure medium [43].

By combining the structural characterization and transport results mentioned above, we constructed a phase diagram to elucidate the pressure tuning of the structure-property relationship in penta-PdPSe, as shown in Fig. 5. It clearly evidences the structural origin of the unusual evolution of electrical and photoelectronic properties. Firstly, the pressure-induced crystalline-amorphous transition occurs at a low critical pressure P_c of around 25 GPa. At P_c, metallization and onset superconducting transition are immediately observed, along with the disappearance of enhanced photoresponse in pristine crystalline phase. Generally, amorphous structure with disorder will induce carrier scattering and additional recombination channels [44,45]. Thus, the formation of a
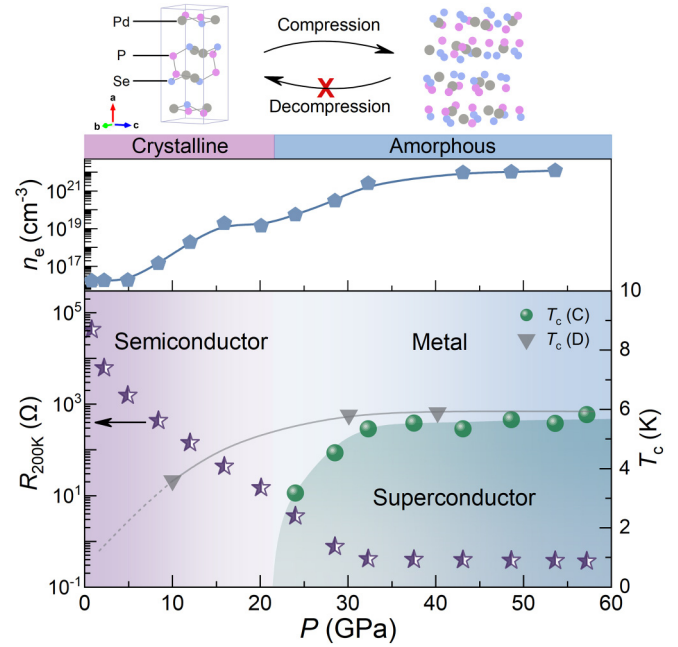

FIG. 5. Relationship between the structural and electronic properties in pressurized penta-PdPSe. (a) Pristine orthorhombic structure and high-pressure amorphous phase. (b) The extracted pressure-dependent charge-carrier density at 10 K. The red cross denotes the irreversibility of phase transition. (c) Pressure dependence of resistance at 200 K (dark-purple stars) and the superconducting transition temperature T_c (green balls and gray triangles). T_c value is defined as the onset temperature of the superconducting transition. The colored areas denote different electronic states along with the different crystal structures. The different colored areas distinguish the electrical states of semiconductor, metal, and superconductor. The green and gray symbols denote the data from the compression and decompression processes, respectively. The dashed lines below 10 GPa are a guide to the eye.

high-pressure amorphous phase is responsible for the emergence of the sudden disappearance of photocurrent. Note that the critical temperature T_c initially increases above P_c and the superconductivity is robust over 30 GPa, in accordance with the trend of charge density versus pressure. Secondly, the amorphous structure is retained during decompression, signaling the irreversibility of crystalline-amorphous transition after a compression-decompression cycle. This structural irreversibility is consistently reflected by the preserved metallic conductivity, as well as the featureless Raman modes. Note that different from the crystalline-to-crystalline transitions in its parent material PdSe$_2$ and predicted orthorhombic-monoclinic phase transition in the isostructural PdPS, PdPSe displays unique amorphization routes with applying high pressure [22–24]. On the other hand, the strong relevance between amorphization and superconductivity are also reported in other low-dimensional materials, such as one-dimensional (TaSe$_4$)$_2$I and (NbSe$_4$)$_2$I [46,47], and Pd-based kagome phosphochalcogenide Pd$_3$P$_2$S$_8$ [43,48]. For instance, Wang *et al.* showed the amorphous transition in kagome Pd$_3$P$_2$S$_8$ as a result of structural instability arising from the increased coupling of Pd and S atoms between adjacent

layers under high pressure [48]. Further investigations are needed to understand the structural evolution in pressurized penta-PdPX (X = S, Se).

IV. CONCLUSION

In summary, by combining synchrotron x-ray diffraction, Raman scattering, electrical transport, photoelectric response experiments, and theoretical calculations, we constructed the relationship between the structural, photoelectronic, and electrical properties of the bulk pentagonal semiconductor PdPSe. We observe the pressure-induced structural phase transition, metallization, and superconductivity, as well as enhancement of photocurrent. After applying external pressure, metallization and superconductivity simultaneously appear, which is concomitant with a sudden disappearance of photocurrent. This behavior can be attributed to the appearance of a crystalline-amorphous transition. During the decompression process, the metallic conductivity is preserved near ambient pressure in depressurized PdPSe, due to the irreversibility of phase transition.

[1] K. S. Novoselov, A. Mishchenko, A. Carvalho, and A. H. Castro Neto, 2D materials and van der Waals heterostructures, Science **353**, aac9439 (2016).

[2] A. K. Geim, Graphene: Status and prospects, Science **324**, 1530 (2009).

[3] S. Zhang, J. Zhou, Q. Wang, X. Chen, Y. Kawazoe, and P. Jena, Penta-graphene: A new carbon allotrope, Proc. Natl. Acad. Sci. USA **112**, 2372 (2015).

[4] Y. Shen and Q. Wang, Pentagon-based 2D materials: Classification, properties and applications, Phys. Rep. **964**, 1 (2022).

[5] M. A. Nazir, A. Hassan, Y. Shen, and Q. Wang, Research progress on penta-graphene and its related materials: Properties and applications, Nano Today **44**, 101501 (2022).

[6] S. Zhang and B. Liu, Hole-doping-induced half-metallic ferromagnetism in a highly-air-stable PdSe$_2$ monolayer under uniaxial stress, J. Mater. Chem. C **6**, 6792 (2018).

[7] Q. Liang, Z. Chen, Q. Zhang, and A. T. S. Wee, Pentagonal 2D transition metal dichalcogenides: PdSe$_2$ and beyond, Adv. Funct. Mater. **32**, 2203555 (2022).

[8] J. Li, X. Fan, Y. Wei, H. Liu, S. Li, P. Zhao, and G. Chen, Half-metallicity and ferromagnetism in *penta*-AlN$_2$ nanostructure, Sci. Rep. **6**, 33060 (2016).

[9] K. Zhao, Y. Guo, Y. Shen, Q. Wang, Y. Kawazoe, and P. Jena, Penta-BCN: A new ternary pentagonal monolayer with intrinsic piezoelectricity, J. Phys. Chem. Lett. **11**, 3501 (2020).

[10] Q. Liang, Q. Wang, Q. Zhang, J. Wei, S. X. Lim, R. Zhu, J. Hu, W. Wei, C. Lee, C. Sow, W. Zhang, and A. T. S. Wee, High-performance, room temperature, ultra-broadband photodetectors based on air-stable PdSe$_2$, Adv. Mater. **31**, e1807609 (2019).

[11] A. D. Oyedele, S. Yang, L. Liang, A. A. Puretzky, K. Wang, J. Zhang, P. Yu, P. R. Pudasaini, A. W. Ghosh, Z. Liu, C. M. Rouleau, B. G. Sumpter, M. F. Chisholm, W. Zhou, P. D. Rack, D. B. Geohegan, and K. Xiao, PdSe$_2$: Pentagonal

two-dimensional layers with high air stability for electronics, J. Am. Chem. Soc. **139**, 14090 (2017).

[12] Y. Gu, H. Cai, J. Dong, Y. Yu, A. N. Hoffman, C. Liu, A. D. Oyedele, Y. C. Lin, Z. Ge, A. A. Puretzky, G. Duscher, M. F. Chisholm, P. D. Rack, C. M. Rouleau, Z. Gai, X. Meng, F. Ding, D. B. Geohegan, and K. Xiao, Two-dimensional palladium diselenide with strong in-plane optical anisotropy and high mobility grown by chemical vapor deposition, Adv. Mater. **32**, e1906238 (2020).

[13] R. Duan, C. Zhu, Q. Zeng, X. Wang, Y. Gao, Y. Deng, Y. He, J. Yang, J. Zhou, M. Xu, and Z. Liu, PdSe: Component-fusion-based topology designer of two-dimensional semiconductor, Adv. Funct. Mater. **31**, 2102943 (2021).

[14] P. Li, J. Zhang, C. Zhu, W. Shen, C. Hu, W. Fu, L. Yan, L. Zhou, L. Zheng, H. Lei, Z. Liu, W. Zhao, P. Gao, P. Yu, and G. Yang, Penta-PdPSe: A new 2D pentagonal material with highly in-plane optical, electronic, and optoelectronic anisotropy, Adv. Mater. **33**, 2102541 (2021).

[15] B. Mortazavi, M. Shahrokhi, X. Zhuang, T. Rabczuk, and A. V. Shapeev, Mechanical, thermal transport, electronic and photocatalytic properties of penta-PdPS, -PdPSe and -PdPTe monolayers explored by first-principles calculations, J. Mater. Chem. C **10**, 329 (2022).

[16] Y. Jing, Y. Ma, Y. Wang, Y. Li, and T. Heine, Ultrathin layers of PdPX (X = S, Se): Two dimensional semiconductors for photocatalytic water splitting, Chem. Eur. J. **23**, 13612 (2017).

[17] A. Aasi, B. Mortazavi, and B. Panchapakesan, Two-dimensional PdPS and PdPSe nanosheets: Novel promising sensing platforms for harmful gas molecules, Appl. Surf. Sci. **579**, 152115 (2022).

[18] A. Di Bartolomeo, A. Pelella, X. Liu, F. Miao, M. Passacantando, F. Giubileo, A. Grillo, L. Iemmo, F. Urban, and S. J. Liang, Pressure-tunable ambipolar conduction and hysteresis in thin palladium diselenide field effect transistors, Adv. Funct. Mater. **29**, 1902483 (2019).

[19] G. Liu, L. Kong, J. Gong, W. Yang, H. Mao, Q. Hu, Z. Liu, R. D. Schaller, D. Zhang, and T. Xu, Pressure-induced bandgap optimization in lead-based perovskites with prolonged carrier lifetime and ambient retainability, Adv. Funct. Mater. **27**, 1604208 (2016).

[20] Z. Chi, X. Chen, F. Yen, F. Peng, Y. Zhou, J. Zhu, Y. Zhang, X. Liu, C. Lin, S. Chu, Y. Li, J. Zhao, T. Kagayama, Y. Ma, and Z. Yang, Superconductivity in pristine 2Ha-MoS$_2$ at ultra-high pressure, Phys. Rev. Lett. **120**, 037002 (2018).

[21] Y. Yuan, Z. Zhang, W. Wang, Y. Zhou, X. Chen, C. An, R. Zhang, Y. Zhou, C. Gu, L. Li, X. Li, and Z. Yang, Pressure-induced enhancement of optoelectronic properties in PtS$_2$, Chin. Phys. B **27**, 066201 (2018).

[22] M. A. ElGhazali, P. G. Naumov, H. Mirhosseini, V. Süß, L. Müchler, W. Schnelle, C. Felser, and S. A. Medvedev, Pressure-induced superconductivity up to 13.1 K in the pyrite phase of palladium diselenide PdSe$_2$, Phys. Rev. B **96**, 060509(R) (2017).

[23] C. Soulard, X. Rocquefelte, P. E. Petit, M. Evain, S. Jobic, J. P. Itie, P. Munsch, and M. H. Whangbo, Experimental and theoretical investigation on the relative stability of the PdS$_2$- and pyrite-type structures of PdSe$_2$, Inorg. Chem. **43**, 1943 (2004).

[24] S. N. Gupta, A. Singh, S. Sarkar, D. V. S. Muthu, S. Sampath, U. Waghmare, and A. K. Sood, Pressure-induced electronic and isostructural phase transitions in PdPS: Raman, x-ray, and first-principles study, Phys. Rev. B **101**, 035123 (2020).

[25] Y. Yuan, X. Zhu, Y. Zhou, X. Chen, C. An, Y. Zhou, R. Zhang, C. Gu, L. Zhang, X. Li, and Z. Yang, Pressure-engineered optical properties and emergent superconductivity in chalcopyrite semiconductor ZnSiP$_2$, NPG Asia Mater. **13**, 15 (2021).

[26] H. K. Mao, J. Xu, and P. M. Bell, Calibration of the ruby pressure gauge to 800 kbar under quasi-hydrostatic conditions, J. Geophys. Res. **91**, 4673 (1986).

[27] J. P. Perdew, K. Burke, and M. Ernzerhof, Generalized gradient approximation made simple, Phys. Rev. Lett. **77**, 3865 (1996).

[28] G. Kresse and D. Joubert, From ultrasoft pseudopotentials to the projector augmented-wave method, Phys. Rev. B **59**, 1758 (1999).

[29] G. Kresse and J. Furthmuller, Efficient iterative schemes for *ab initio* total-energy calculations using a plane-wave basis set, Phys. Rev. B **54**, 11169 (1996).

[30] S. Baroni, S. Gironcoli, A. D. Corso, and P. Giannozzi, Phonons and related crystal properties from density-functional perturbation theory, Rev. Mod. Phys. **73**, 515 (2001).

[31] A. Togo and I. Tanaka, First principles phonon calculations in materials science, Scr. Mater. **108**, 1 (2015).

[32] T. A. Bither, P. C. Donohue, and H. S. Young, Palladium and platinum phosphochalcogenides—Synthesis and properties, J. Solid State Chem. **3**, 300 (1971).

[33] J. V. Marzik, R. Kershaw, K. Dwight, and A. Wold, Preparation and properties of PdPSe single crystals, J. Solid State Chem. **44**, 382 (1982).

[34] P. Cheng, T. Ye, J. Yan, K. Zhang, D. Yao, X. Pan, Y. Wang, E. Xue, F. Su, J. Zhang, and J. Ding, Semiconductor-semimetal transition-driven photocurrent spurt and infrared band response

in lead iodide at high pressure, Adv. Opt. Mater. **11**, 2300316 (2023).

[35] P. Wang, Y. Wang, J. Qu, Q. Zhu, W. Yang, J. Zhu, L. Wang, W. Zhang, D. He, and Y. Zhao, Pressure-induced structural and electronic transitions, metallization, and enhanced visible-light responsiveness in layered rhenium disulphide, Phys. Rev. B **97**, 235202 (2018).

[36] A. P. Nayak, S. Bhattacharyya, J. Zhu, J. Liu, X. Wu, T. Pandey, C. Jin, A. K. Singh, D. Akinwande, and J. F. Lin, Pressure-induced semiconducting to metallic transition in multilayered molybdenum disulphide, Nat. Commun. **5**, 3731 (2014).

[37] Z. Li, R. Liu, Q. Li, and B. Liu, Photoelectric properties of functional materials under high pressure, Adv. Phys. Res. **2**, 2200102 (2023).

[38] X. Lu, Y. Wang, C. C. Stoumpos, Q. Hu, X. Guo, H. Chen, L. Yang, J. S. Smith, W. Yang, Y. Zhao, H. Xu, M. G. Kanatzidis, and Q. Jia, Enhanced structural stability and photo responsiveness of CH$_3$NH$_3$SnI$_3$ perovskite via pressure-induced amorphization and recrystallization, Adv. Mater. **28**, 8663 (2016).

[39] V. L. Ginzburg and L. D. Landau, On the theory of superconductivity, Zh. Eksp. Teor. Fiz. **20**, 1064 (1950) .

[40] F. Birch, Finite elastic strain of cubic crystals, Phys. Rev. **71**, 809 (1947).

[41] R. Kempt, A. Kuc, and T. Heine, Two-dimensional noble-metal chalcogenides and phosphochalcogenides, Angew. Chem., Int. Ed. **59**, 9242 (2020).

[42] A. F. Goncharov and V. V. Struzhkin, Raman spectroscopy of metals, high-temperature superconductors and related materials under high pressure, J. Raman Spectrosc. **34**, 532 (2003).

[43] Y. Zhou, X. He, S. Wang, J. Wang, X. Chen, Y. Zhou, C. An, M. Zhang, Z. Zhang, and Z. Yang, Pressure-induced superconductivity in the kagome single-crystal Pd$_3$P$_2$S$_8$, Phys. Rev. B **106**, 104512 (2022).

[44] S. Guo, K. Bu, J. Li, Q. Hu, H. Luo, Y. He, Y. Wu, D. Zhang, Y. Zhao, W. Yang, M. G. Kanatzidis, and X. Lu, Enhanced photocurrent of all-inorganic two-dimensional perovskite Cs$_2$PbI$_2$Cl$_2$ via pressure-regulated excitonic features, J. Am. Chem. Soc. **143**, 2545 (2021).

[45] Y. Wang, C. Liu, Y. Ren, X. Zuo, S. E. Canton, K. Zheng, K. Lu, X. Lv, W. Yang, and X. Zhang, Visualizing light-induced microstrain and phase transition in lead-free perovskites using time-resolved x-ray diffraction, J. Am. Chem. Soc. **144**, 5335 (2022).

[46] C. An, Y. Zhou, C. Chen, F. Fei, F. Song, C. Park, J. Zhou, H. G. Rubahn, V. V. Moshchalkov, X. Chen, G. Zhang, and Z. Yang, Long-range ordered amorphous atomic chains as building blocks of a superconducting quasi-one-dimensional crystal, Adv. Mater. **32**, e2002352 (2020).

[47] C. Pei, W. Shi, Y. Zhao, L. Gao, J. Gao, Y. Li, H. Zhu, Q. Zhang, N. Yu, C. Li, W. Cao, S. A. Medvedev, C. Felser, B. Yan, Z. Liu, Y. Chen, Z. Wang, and Y. Qi, Pressure-induced a partial disorder and superconductivity in quasi-one-dimensional Weyl semimetal (NbSe$_4$)$_2$I, Mater. Today Phys. **21**, 100509 (2021).

[48] Q. Wang, X. Qiu, C. Pei, B. Gong, L. Gao, Y. Zhao, W. Cao, C. Li, S. Zhu, M. Zhang, Y. Chen, K. Liu, and Y. Qi, Superconductivity emerging from a pressurized van der Waals kagome material Pd$_3$P$_2$S$_8$, New J. Phys. **25**, 043001 (2023).